



Probing Charge Transfer in a Novel Class of Luminescent Perovskite-Based Heterostructures Composed of Quantum Dots Bound to RE-Activated CaTiO₃ Phosphors

Journal:	<i>Nanoscale</i>
Manuscript ID	NR-ART-09-2015-006697.R1
Article Type:	Paper
Date Submitted by the Author:	06-Nov-2015
Complete List of Authors:	Lewis, Crystal; Chemistry, Liu, Haiqing; Stony Brook University, Han, Jinkyu; SUNY Stony Brook, Wang, Lei; SUNY Stony Brook, Yue, Shiyu; Chemistry, Brennan, Nicholas; Stony Brook University, Wong, Stanislaus S; SUNY Stony Brook,

**Probing Charge Transfer in a Novel Class of Luminescent Perovskite-Based
Heterostructures Composed of Quantum Dots Bound to RE-Activated CaTiO₃ Phosphors**

Crystal S. Lewis¹, Haiqing Liu¹, Jinkyu Han², Lei Wang¹, Shiyu Yue¹, Nicholas A. Brennan¹,
and Stanislaus S. Wong^{1,2*}

¹Department of Chemistry, State University of New York at Stony Brook,
Stony Brook, NY 11794-3400

²Condensed Matter of Physics and Materials Sciences Department,
Brookhaven National Laboratory, Building 480; Upton, NY 11973

*To whom correspondence should be addressed.

Email: Stanislaus.wong@stonybrook.edu; sswong@bnl.gov

Phone: 631-632-1703; 631-344-3178

Abstract

We report on the synthesis and structural characterization of novel semiconducting heterostructures composed of cadmium selenide (CdSe) quantum dots (QDs) attached onto the surfaces of novel high-surface area, porous rare-earth-ion doped alkaline earth titanate micron-scale spherical motifs, i.e. both Eu-doped and Pr-doped CaTiO₃, composed of constituent, component nanoparticles. These unique metal oxide perovskite building blocks were created by a multi-pronged synthetic strategy involving molten salt and hydrothermal protocols. Subsequently, optical characterization of these heterostructures indicated a clear behavioral dependence of charge transfer in these systems upon a number of parameters such as the nature of the dopant, the reaction temperature, and particle size. Specifically, 2.7 nm diameter ligand-functionalized CdSe QDs were anchored onto sub-micron sized CaTiO₃-based spherical assemblies, prepared by hydrothermal methodologies. We found that both the Pr- and Eu-doped CaTiO₃ displayed pronounced PL emissions, with maximum intensities observed using optimized lanthanide concentrations of 0.2 mol% and 6% mol, respectively. Analogous experiments were performed on Eu doped BaTiO₃ and SrTiO₃ oxide motifs, but CaTiO₃ still performed as the most effective host material amongst the three perovskite systems tested. Moreover, the ligand-capped CdSe QD – doped CaTiO₃ heterostructures exhibited effective charge transfer between the two individual constituent nanoscale components, an assertion corroborated by the corresponding quenching of their measured PL signals.

Keywords: CaTiO₃, praseodymium, europium, rare earth ion-doped materials, doped perovskites, metal titanates, fluorescent and luminescent materials, optical properties

1. Introduction

In recent years, ternary, including either ABO_3 or ABO_4 compositions, metal oxides have been extensively investigated as a result of their exceptional dielectric, ferroelectric, pyroelectric, piezoelectric, magnetic, and semiconducting properties with possible applications as components in solid oxide fuel cells, gas sensors, steam electrolysis units, and photocatalysts for water splitting.^{1,2} In particular, within the ABO_3 perovskite structure, the A site cation is located in a 12-coordinated cubic octahedral geometry, while the B site cation is 6-fold coordinated with oxygen anions positioned within an octahedral geometry. Typically the larger cation resides in the A site, whereas the smaller cation is located in the center of the octahedra as the B site.^{3,4}

Various techniques, such as co-precipitation, impregnation, in situ preparation methods, microwave, sol-gel, solvothermal, hydrothermal, molten salt, and solid state-based syntheses have been employed to synthesize a number of classes of perovskites.⁵⁻⁹ In particular, our lab has successfully achieved the generation of various motifs (i.e. nanotubes, nanowires, nanocubes, and nanoparticles) of the ABO_3 perovskite system, including $BiFeO_3$, $LiNbO_3$, $BaZrO_3$, $BaTiO_3$, $SrTiO_3$, and $SrRuO_3$ using facile and readily scalable techniques such as but not limited to sol-gel, hydrothermal, and molten salt type reactions as well as a combination thereof.¹⁰⁻¹⁴

Among these ABO_3 systems is the orthorhombic phase of calcium titanate ($CaTiO_3$), possessing a space group of $Pnma$. $CaTiO_3$ is a particularly important perovskite, due to its biocompatibility, and has been used for example as a coating for Ti implants.^{15,16} Moreover, as a result of its wide band gap energy of ~ 3.7 eV,^{16,17} it has also been incorporated as a component of functional electronic devices.¹⁸ In addition, it is also a key constituent of a synthetic rock known as Synroc, which is used to immobilize nuclear waste.^{19,20} Furthermore, it is a typical incipient ferroelectric whose dielectric constant increases with decreasing temperatures, i.e. from

$\epsilon_r \approx 170$ at 300 K to $\epsilon_r \approx 330$ at 4.2 K, thereby leading to possible, potential applications in microwave devices.^{20, 21}

Though these perovskite structures are relatively stable, the A and/or B site cation may undergo lattice substitution with foreign cations maintaining either a distinctive oxidation state or a singular ionic radius, while preserving its inherent crystalline structure.⁵ Not surprisingly, a number of perovskite-type oxides, i.e. ABO_3 (with 'A' = Ca, Sr, or Ba; 'B' = Ti, Zr, or Si), have served as the host material for rare-earth-ion (RE) activators, such as Pr^{3+} , Eu^{3+} , and Tb^{3+} , and have evinced intense red and blue-green luminescent properties, depending on the identity of the dopant itself.^{17, 18, 22-24} Specifically, red-emitting phosphors, incorporating Pr^{3+} and Eu^{3+} , are being explored for their applications in cathode ray tube (CRT) television displays.²⁵ Moreover, $CaTiO_3$ has also operated as a potential host lattice for large to medium-sized RE ions (i.e. La to Eu), which either selectively dope at the Ca-site via a Ca vacancy incorporation mechanism or integrate via a charge compensation mechanism wherein RE ions substitute at both the Ca and Ti sites within the $CaTiO_3$ lattice structure, according to theoretical calculations.²⁰

In general, the enhanced luminescent properties, observed within the combined host-rare earth ion dopant system, originates from UV light-mediated promotion of an electron from the ground state of the host to the excited $5d$ state of the RE ion, which overlaps with the conduction band of the host. As a result, the electron can completely delocalize within the conduction band and auto-ionize (i.e. through emission of the outer shell electrons), thereby giving rise to a state involving the simultaneous generation of Ln^{3+} , h^+ , and free e^- . The capture of the free electron results in energy emission due to excitonic recombination with some of the energy transferred to the re-emitting lanthanide $4f$ state.^{6, 26}

In an effort to potentially control and further enhance these desirable luminescent properties, studies have sought to alter the concentration of the rare earth ion, to vary the synthesis reaction temperature, as well as to add in co-dopant species (such as Bi^{3+}).^{6,27} However, direct correlations between the synthesis technique and the resulting luminescence have yet to be thoroughly explored. The closest analogue to the current study in terms of intellectual direction and stated objectives is a recent work on calcium apatite nanoparticles (~50 nm) which had been either electrostatically adsorbed or grown in situ onto ~200 nm silica particles; interpretation of the optical data on these systems did not yield any perceptible difference in the luminescence behavior either in the presence or absence of the silica spheres.²⁸

Therefore, our study is significant for three main reasons. *First*, to highlight the robustness and relative ease of formation of our heterostructures, we have focused on creating well defined and previously unreported motifs of RE-doped CaTiO_3 prepared using two distinctive and complementary methodologies, i.e. molten salt and hydrothermal syntheses. Interestingly, each methodology possesses its own advantages and disadvantages. For example, the molten salt method generates relatively high yields of products (minimum of ~200 mg per run) and enables the simple, scalable, and cost-effective production of highly crystalline materials,⁶ This protocol also gives rise to disadvantages, such as insufficient size control and high nucleation rates, thereby resulting in agglomeration. By contrast, the hydrothermal method can lead not only to the production of crystalline, phase pure materials with little if any perceptible defects but also to the fabrication of novel size-controlled morphologies. However, the size and shape distribution of materials prepared hydrothermally may be polydisperse.²

Second, we have synthesized novel heterostructures, comprised of cadmium selenide (CdSe) quantum dots (QDs) immobilized onto porous RE (RE = Eu and Pr) - doped CaTiO_3

micron-scale structures, the last of which have been fabricated using the molten salt technique. Based on our previous investigations, particularly with QDs attached onto carbon nanotubes (CNTs), we have observed that coupling constituent moieties with unique size and composition-dependent properties can yield products with unforeseen characteristics as compared with their individual components.^{29,30} This observation has been the underlying theme of our systematic efforts to create novel and optically intriguing heterostructures created by attaching CdSe and CdS QDs onto various nanoscale motifs of (a) CePO₄, (b) LaPO₄, (c) CaWO₄ as well as (d) calcium tungstate/molybdate-based systems, which had been doped with RE (with RE = Eu, Ce, and/or Tb).³¹⁻³⁴ In that series of studies, we independently probed the effects of chemical composition, dopant identity, coverage, and morphology upon the resulting optical behavior.

Third, it is worth mentioning that there have been only two prior reports on heterostructures, composed of as-prepared QDs coupled with perovskites, and these had been tailored for water splitting applications. Specifically, CdSe-SrTiO₃ and CdS-BaSnO₃ composite heterostructures gave rise to improved photoelectrochemical performances with photocurrent densities of ~ 5 mA/cm² and ~ 4.8 mA/cm² at 0 V, respectively.^{35,36} Herein, our emphasis is different and distinctive in that we have (i) purposely generated novel, previously unreported, crystalline, and porous spherical motifs of CaTiO₃ and (ii) subsequently taken advantage of the favorable luminescent characteristics of their doped analogues to create unusual perovskite-based heterostructures with unique optoelectronic properties. Moreover, we have sought to more precisely understand the nature of the charge transfer properties within these systems.

Hence, in this study, previously unreported porous spherical motifs of Eu and Pr-doped CaTiO₃ micron-scale structures have been prepared using both customized molten salt as well as modified hydrothermal methods. The photoluminescent properties of these materials were

separately measured and compared. We found that the molten salt method gave rise to metal oxides characterized by clearly superior photoluminescence performance as compared with hydrothermally derived samples. Therefore, for our subsequent photophysical studies, CdSe QDs were coupled onto the outer surfaces of these RE doped CaTiO_3 motifs, prepared via the molten salt method, so as to correlate luminescence and charge transfer behavior with structure and morphology within these systems.

2. Experimental

2.1. Materials and Reagents. We used calcium oxalate (99.9%, Aldrich), calcium chloride dihydrate (99-105%, Alfa Aesar), titanium (IV) dioxide (99.8%, Aldrich), titanium foil (99.7%, Strem Chemicals), sodium chloride (EM Reagents), praseodymium (III) chloride hexahydrate (99.9%, Aldrich), Triton X-100 (EMD Industries), sodium hydroxide (99%, EMD Industries), hydrogen peroxide (30%, BHD), cadmium oxide (99%, Acros Organics), selenium (99.5+%, Aldrich), trioctylphosphine oxide (99%, Acros Organics), tributylphosphine, hexadecylamine (90%, Acros Organics), dioctylamine (97%, Acros Organics), and 3-mercaptopropionic acid (99+%, Acros Organics) as reagents without additional purification.

2.2. Methodology.

2.2.1. (RE = Pr and Eu) doped CaTiO_3 porous micron-scale spheres - Molten Salt Method

To prepare Re-doped CaTiO_3 using a molten salt method, we followed a typical synthesis, wherein calcium oxalate, titanium dioxide (bulk TiO_2), sodium chloride (NaCl), and Triton X-100 were mixed together with an overall molar ratio of 1: 1: 20: 3, and ground for 30 minutes. Various molar dopant percentages 'x' of either praseodymium chloride (PrCl_3) (with 'x' = 0.05, 0.1, 0.2, and 0.5) or europium nitrate $\text{Eu}(\text{NO}_3)_3$ (with 'x' = 2, 4, and 6) were subsequently

added to the slurry solution and ground for 30 minutes. Afterwards, the mixture was then placed in a quartz crucible and inserted into the muffle furnace, where it was annealed at 820°C for 3.5 h and subsequently cooled to room temperature. The sample was then collected (~200 mg), washed three times in distilled water and once in ethanol (EtOH), and finally desiccated overnight at 80°C in a drying oven.

As for comparable Eu-doped SrTiO₃ and BaTiO₃ perovskites, a previously used molten salt method was employed.¹³ Briefly, strontium or barium oxalate, bulk TiO₂, NaCl, and NP-9 were mixed together with overall molar ratios of 1: 1: 20: 3, respectively. An optimal 6 mol % of Eu was added to the reaction mixture, ground for 30 minutes, and placed within the crucible. Subsequently, the crucible was transferred into the muffle furnace at 820°C for 3.5 hours. After heat treatment, the sample was washed 3x in distilled water, once more in ethanol, and ultimately placed in a drying oven at 80°C.

2.2.2. Re-doped CaTiO₃ porous micron-scale spheres – Hydrothermal Method

With respect to the hydrothermal method, the (RE = Pr and Eu) doped CaTiO₃ were prepared by placing 10 pieces of titanium (Ti) foil as the Ti precursor within a 125 mL Teflon holder. 1 M sodium hydroxide (NaOH) was subsequently added to the Teflon cup followed by the addition of 0.25 M calcium chloride (CaCl₂) to the mixture with stirring for 10 minutes. As an additional oxidizing agent, 7.83 mL of hydrogen peroxide (H₂O₂) was inserted with subsequent stirring for 10 more minutes. Subsequently, dopant molar percentages of either PrCl₃ (i.e. 'x' = 0.2) or Eu(NO₃)₃ (i.e. 'x' = 6) respectively, denoting optimal concentrations from the photoluminescence perspective, were added in the reaction mixture, and stirred for 15 minutes. The Teflon cup containing the reagents was then transferred into the metal autoclave and heated to 180°C for 10 hours. Once the reaction was complete, the sample was collected and washed

twice with not only distilled water but also 2% hydrochloric acid (HCl) to remove calcium oxide impurities, as well as once in EtOH. The sample was subsequently dried overnight at 80°C.

2.2.3. Quantum Dot (QD) Synthesis

The synthesis preparation of CdSe QDs was modified from an existing literature protocol.³⁹ Briefly, 0.2 mmol of CdO and 0.8 mmol of stearic acid were added to a three-necked round bottom flask, then degassed, and ultimately heated at 150°C under an Ar atmosphere. Once the contents were dissolved, 3.88 g each of trioctylphosphine oxide (TOPO) and hexadecylamine (HDA) were added to the flask and heated to 320°C. Separately, a precursor selenium (Se) solution was prepared in an air-sensitive glovebox environment wherein the Se was dissolved in tributylphosphine (TBP) and dioctylamine (DOA). Once the solution mixture had attained 320°C within the flask, the Se precursor was injected therein, and QD growth was allowed to proceed for 15 seconds at 270°C. After growth was achieved, the mixture was later cooled to room temperature, then washed with either methanol (MeOH) or acetone, and ultimately stored in hexane.

2.2.4. Ligand Exchange of QDs & Subsequent Formation of QD – Perovskite titanate: Re Heterostructures

CdSe QDs capped with 3-mercaptopropionic acid (MPA) were synthesized through a ligand exchange reaction. In a typical experiment, a solution of MPA (1 mmol) in 2 ml of MeOH was added to a suspension of as-prepared, capped CdSe QDs (0.04 mmol) in 4 ml of hexane. After stirring for 10 min, QDs were visibly precipitated upon ligand exchange. These QDs were later collected by centrifugation and then washed with both ethanol and MeOH. The resulting QDs were finally re-dispersed in MeOH for further characterization.

In separate runs, MPA-capped CdSe QDs were attached onto molten salt-generated CaTiO₃, SrTiO₃, and BaTiO₃: Re (RE = Pr and Eu) porous micron-scale spheres. From our

preliminary data, we found that these molten salt-derived samples yielded the most reproducible PL data with the highest emission intensities reported. This interaction occurred presumably through a hydrogen bonding mechanism involving the hydroxyl and acid-based groups of MPA, adsorbed onto the surfaces of the Re-doped perovskite structure. This strategy was similar to our previous reports of CdSe QDs attached onto CePO_4 : Tb nanowires as well as onto LaPO_4 : RE (RE = Eu, Ce, and Tb) nanostructures.^{31, 32} In a typical experiment, 2.4 mg (10.4 μmol) of CaTiO_3 : RE motifs in 2 ml MeOH was added to 2 mg (10.4 μmol) of MPA-capped CdSe QDs in 2 ml of MeOH. The resulting solution was subsequently sonicated and stirred in the dark for 10 min and 2 h, respectively, so as to preserve optical integrity. These as-prepared heterostructures, which had been dispersed in MeOH, were used for further characterization and analysis.

2.3. Characterization

2.3.1. X-ray Diffraction (XRD)

The crystallographic purity of as-prepared QD-Pr- CaTiO_3 was confirmed using powder XRD. To prepare a typical sample for analysis, a fixed quantity was dispersed in ethanol, sonicated for ~ 1 min, and then air-dried upon deposition onto the sample holder. Diffraction patterns were subsequently obtained using Rigaku Miniflex diffractometer, operating in the Bragg configuration using Cu $K\alpha$ radiation (1.54 Å) and 2θ lattice parameters, ranging from 20 to 80° at a scanning rate of 1.0°/min for variously RE doped CaTiO_3 .

2.3.2. Electron Microscopy

The specific morphologies and sizes of the perovskite micron-scale spheres were probed using a field emission scanning electron microscope (FE-SEM Leo 1550) as well as an analytical high resolution SEM (JEOL 7600F) instrument, operating at an accelerating voltage of 15 kV, both of which were equipped with EDAX capabilities. To prepare these samples for structural

characterization, fixed amounts were dispersed in ethanol and sonicated for ~1 min, prior to their deposition onto a silicon (Si) wafer.

Low magnification transmission electron microscope (TEM) was also used at an accelerating voltage of 120 kV with the JEOL JEM-1400 instrument, equipped not only with a 2048 x 2048 Gatan CCD Digital Camera but also energy dispersive spectroscopy (EDS) mapping capabilities. High-resolution TEM images coupled with selected area electron diffraction (SAED) patterns were collected at an accelerating voltage of 200 kV on a JEOL JEM-2100F microscope outfitted with a Gatan Tridiem energy imaging filter. Similar sample preparations for microscopy analysis were initiated using an ethanolic dispersion followed by sonication. Subsequently, the solution was deposited drop-wise onto a 300 mesh Cu grid.

2.3.3. BET Analysis

Samples prepared for BET analysis were initially dried in an oven to remove any residual solvents. Subsequently, ~100 mg of as-prepared perovskite material as well as the corresponding anatase TiO₂ standard reference material (i.e. surface area $\sim 10.24 \pm 0.54 \text{ m}^2/\text{g}$) were each placed within an individual analysis tube and de-gassed for 2 hours at 150°C in order to remove any adsorbed species from the particles' surfaces. After de-gassing, a BET surface area analysis was conducted using a Quantachrome Nova 2200e Series Instrument through the mediation of a 10-point sampling method.

2.3.4. Fourier Transform Infrared Spectroscopy (FT-IR)

FT-IR spectral data were acquired on a Nexus 670 instrument (ThermoNicolet), equipped with a Smart Orbit diamond ATR accessory, consisting of a KBr beam splitter and a DTGS KBr detector. As-prepared powder samples were placed onto the crystal surface. A 64-scan background correction in air was performed in the spectral range studied. FT-IR data were

typically recorded (~64 scans) over the wavenumber range of 1000–4000 cm^{-1} and were subsequently evaluated in terms of characteristic, expected absorption bands. Spectra were processed using the Omnic software with a spatial resolution of 1 cm^{-1} .

2.3.5. Optical Spectroscopy

UV-visible spectra were obtained on a ThermoSpectronics UV1 spectrometer using quartz cells possessing a 10 mm path length. Once these as-prepared samples were sonicated in ethanol, spectra were obtained for CdSe QDs, Pr and Eu-doped CaTiO_3 porous micron-scale spherical motifs, as well as the associated heterostructures. Samples for PL spectra were dispersed in methanol (MeOH) for MPA-capped CdSe QDs, CaTiO_3 : RE (RE = Eu and Pr), as well as for associated CdSe QD– CaTiO_3 : Re heterostructures. Fluorescence data of these uniform dispersions were subsequently acquired at room temperature using a FluoroMax-4 spectrofluorimeter (Jobin Yvon) at 15 s and 5 s integration times, using excitation wavelengths of 325 nm and 399 nm for CaTiO_3 : Pr and Eu, respectively. As for the MPA-capped QDs and the resulting CdSe QD - perovskite titanate: Re heterostructures, relevant optical data were obtained using an excitation wavelength of 375 nm.

3. Results & Discussion

3.1. Structural Characterization

3.1.1. Pr-doped CaTiO_3

In our systematic efforts to generate pure, homogeneous, and uniform RE-doped CaTiO_3 , in terms of size, shape, and morphology, we carefully tested and varied a number of reaction parameters such as the molar ratios of titanium precursors, the nature of the surfactants, as well as the reaction times themselves. A summary of our data from these collective runs as well as

from complementary X-Ray diffraction results is presented in the Supplementary Information Table S1 as well as Figures S1 and S2, respectively. In effect, we were able to successfully demonstrate the synthesis of pure Pr doped CaTiO_3 using both the molten salt (MS) and hydrothermal methodologies. The corresponding XRD patterns, shown in Figures 1A and B and associated with both synthetic techniques, unequivocally reveal that our as-prepared samples evinced a pure cubic perovskite structure, possessing a space group of $Pnma$. These findings agree with the JCPDS standard #22-0153 with little if any detectable impurities observed in either sample. Additionally, the crystallite sizes for both hydrothermal and molten salt-prepared perovskites were calculated using the Debye-Scherrer Equation, and these data yielded crystallite domain size dimensions of ~ 29.9 and ~ 38.1 nm, respectively. Upon closer analysis of the XRD spectra (Figure S2), it is evident that for both the molten salt and hydrothermally prepared samples, the Pr replaces the underlying Ca ions, constrains the lattice and results in a peak, which is upshifted to $\sim 33^\circ$.

Moreover, the sizes and morphologies of both molten salt and hydrothermally prepared Pr-doped CaTiO_3 motifs were investigated using a combination of TEM and SEM. With respect to the SEM analysis, representative images are shown in Figures 2A and B. Specifically, Figure 2A can be ascribed to the molten salt-prepared CaTiO_3 : Pr micron-scale spheres, possessing average diameters of 226 ± 30 nm. Analysis of the corresponding TEM image in the inset to Figure 2A yielded average diameters of 210 ± 22 nm, which are consistent with the SEM data. Based upon XRD, it is clear that these structures are composed of constituent ~ 38.1 nm particles closely fused within a spherical motif. From both electron microscopy images, it is moreover clear that the external surfaces of the micron-scale spheres appear to be slightly roughened and corrugated with a surface area of ~ 8.7 m^2/g (Table S2). This magnitude of surface area is

comparable to previous literature reports on perovskites that had been previously prepared at similar reaction temperatures.⁴⁰

As for the hydrothermally synthesized CaTiO_3 : Pr samples, the representative SEM image in Figure 2B confirms the formation of porous micron-scale spheres with average diameters of 330 ± 97 nm. The TEM image in the inset to Figure 2B gives forth similar morphologies maintaining average diameters of 304 ± 85 nm. From these images, it is apparent that the resulting porous micron-scale spheres likely are composed of high-surface-area aggregates, characterized by smaller constituent nanoparticulate units, measuring ~ 29.9 nm, concentrically arranged and assembled. This observation was corroborated by our BET data, wherein our as-prepared perovskites exhibited a relatively large specific surface area of ~ 51.9 m^2/g (Table S2), a finding consistent with the intrinsically porous nature of our CaTiO_3 perovskite structures.⁴¹

In addition, a series of high-resolution TEM (HRTEM) images for both molten salt prepared and hydrothermal treated perovskite samples (i.e. Figures 3B & E) revealed expected interlayer d -spacings, corresponding to the orthorhombic phase of the host material, CaTiO_3 . Specifically, the measured d -spacings of 0.278 nm and 0.279 nm, respectively, were consistent with the anticipated (112) lattice plane within CaTiO_3 . Complementary SAED patterns (Figures 3C & F) highlight the presence of distorted diffraction spots, which can be potentially attributed to the overall polycrystallinity of the micron-scale structures. Nevertheless, careful analysis of the diffraction patterns indicates that the data are consistent with the expected perovskite host material, i.e. CaTiO_3 .

3.1.2. *Eu-doped CaTiO₃*

To deal with the issue of possible dopant-induced structural distortions, we should note that the Eu-doped CaTiO_3 also evinced a pure cubic perovskite structure itself, and that the structural characterization data agreed with the JCPDS standard without the presence of any detectable impurities (Figure 4A). By analogy with the Pr-doped sample, the XRD spectra highlights a upshifted peak position centered at a 2θ value of $\sim 33^\circ$, indicative of a lattice expansion wherein the Eu (~ 109 pm) ion substitutes for the larger Ca (~ 140 pm) ion at the A site. Various molar concentrations of Eu^{3+} have been successfully incorporated within the CaTiO_3 lattice. Based on the XRD data (Figure S3), for all of the molar % concentrations probed, the crystal lattice becomes more spatially constrained, through the preferential replacement of the Ca ion with Eu at the A site.⁴²⁻⁴⁴

The size and morphology of our molten salt-prepared Eu-doped CaTiO_3 motifs were investigated using a combination of TEM and SEM data. With respect to the SEM (Figure 4B), the roughened spherical motifs averaged $\sim 290 \pm 35$ nm in diameter, whereas with TEM (inset of Figure 4B), the structures measured $\sim 315 \pm 27$ nm in diameter. Additionally, the SEM analysis (Figure 5A and C) of a series of analogous Eu-doped Sr and BaTiO_3 microspheres revealed similar size dimensions to that of CaTiO_3 -based motifs, with overall diameters noted to be $\sim 262 \pm 37$ nm and $\sim 243 \pm 32$ nm, respectively. The corresponding XRD patterns, shown in Figures 5B and D, reveal that the chemical compositions of our as-prepared samples agree with the JCPDS standards #73-0661 and #31-0174 with little if any detectable unforeseen impurities observed in either sample analyzed, i.e. Eu-doped SrTiO_3 and BaTiO_3 , respectively.

3.1.3. CdSe QD - Perovskite Heterostructures

Both of the Pr: CaTiO_3 - CdSe and Eu: CaTiO_3 - CdSe heterostructures were formed using a procedure developed by our group and which has been previously utilized and reported

for the creation of composite-based systems.³¹⁻³⁴ According to Figure 6, the CdSe quantum dots immobilized onto the outer surfaces of the CaTiO₃ exist as either small aggregates or clusters of several dots, as opposed to individual QDs. This phenomenon has also been observed in our previous studies, involving ligand exchange and the formation of associated heterostructures. This observation has been attributed to QD aggregation during the ligand exchange process.³¹ High-resolution TEM images have demonstrated that the *d*-spacing of the underlying material, i.e. 0.385 nm, can be well correlated with the (101) lattice plane of CaTiO₃, while the measured *d*-spacings of individual dots within the group of particles can be ascribed to the CdSe (100) lattice plane. Additionally, the indexed selected area electron diffraction (SAED) pattern is consistent with the presence of both CaTiO₃ and CdSe.

STEM images along with their corresponding elemental maps are highlighted in Figures 7A-E and 8A-E, wherein we find an even, uniform, and homogeneous spatial distribution of the various constituent elements (i.e. not only Ca, Ti, and O but also Cd and Se) within the CdSe-modified, Pr and Eu-doped CaTiO₃ heterostructures, which is, as expected. We note that a reduced Cd and Se intensity would likely be indicative of the lower overall concentration of quantum dots and suggestive of a quantitatively decreased particulate coverage onto the underlying titanate motifs. Nevertheless, our data are supportive of a fairly even and spatially uniform distribution of this element within the CaTiO₃ host. Indeed, results on the presence and localization of Pr and Eu elements can be found in the Supplemental Information section, particularly Figures S4 and S5, respectively.

3.2. Optical data collected on Pr-doped CaTiO₃ and Corresponding Heterostructures

The incorporation of Pr³⁺ ions within CaTiO₃ microspheres was further confirmed via PL measurements for samples prepared by both molten salt and hydrothermal methods. Indeed, both

spectra (Figure 9) display red emission peaks, located at ~ 611 nm, corresponding to the 1D_2 to 4H_3 transitions of the Pr^{3+} ion.⁴⁵⁻⁴⁷ However, the PL emission intensity associated with the molten salt sample appears to be $\sim 3x$ greater than that observed for the corresponding hydrothermally prepared perovskite counterpart. This finding may be possibly related to inherent structural differences of the perovskite products themselves, such as variations in the inherent constituent crystallite domain size (i.e. ~ 38 nm versus 29.9 nm, respectively) for instance, associated with the disparate reaction temperatures used to prepare these 2 different samples, namely $820^\circ C$ versus $180^\circ C$ for the molten salt versus hydrothermal reactions respectively.

Upon closer analysis of the relevant XRD data and specifically of the peak positioned at $\sim 33^\circ$, there appears to be a more dramatic upshift associated with the hydrothermal sample as compared with its molten salt-prepared counterpart. These results are consistent with a relatively higher degree of substitution (i.e. 0.2 mol % concentration) of Pr for the underlying Ca framework ions associated with the hydrothermal sample as compared with its molten salt derived analogue (Figure S2). Though each synthesis technique uses the same amount of Pr precursor, it can be inferred based on the XRD peaks, that a decreased Pr concentration is integrated within the molten salt prepared perovskite sample.

Hence, the quantity of Pr in and of itself is insufficient to explain the dramatic increase in the red luminescence. A more plausible explanation for this observed difference in the red emission intensity can be put forth, based upon cumulative XRD and BET analysis. Specifically, we note that the hydrothermally-derived sample maintained a high surface area, a large degree of polycrystallinity, as well as the presence of multiple facets, which may have introduced surface defects, such as oxygen vacancies, that could have acted as surface trap sites for excited electrons within the Pr-doped $CaTiO_3$ itself, thereby potentially inducing unfavorable PL

quenching.⁴⁸ Therefore, based on this insight into sample quality, in order to facilitate our optical data interpretation and analysis, the CdSe QDs were subsequently attached onto pure and crystalline molten salt-prepared samples so as to better understand the nature of potential energy and charge transfer within the resulting heterostructures.

Nonetheless, for both synthesis techniques developed, another PL emission peak was observed at ~563 nm (Figure 9), and this signal could be attributed to electron-hole recombination by energetic defects within the CaTiO₃ matrix. These surface defects (i.e. indicative of structural disorder induced at either a short or intermediate range) are primarily caused by the presence of titanium (Ti³⁺) *d*-orbital surface states appearing at relatively higher oxygen vacancy concentrations.^{49, 50} Moreover, the PL emission peak of the bare CaTiO₃ was observed at ~561 nm (Figure S6), again further confirming the expected identity of the peak profile associated with Pr-doped CaTiO₃ samples.⁴⁹

Additionally, PL emission spectra were collected on various mole percent concentrations (i.e. 'x' = 0.05, 0.1, 0.2, and 0.5) of Pr³⁺-doped CaTiO₃ materials, obtained using an excitation wavelength of 325 nm, as shown in Figure 10. By analogy with previous Pr-doped CaTiO₃ samples analyzed in the literature, the PL emission resulted in peaks positioned at ~563 and ~611 nm, corresponding to the intrinsic CaTiO₃ perovskite structure and to the ¹D₂ to ³H₄ transition of Pr³⁺, respectively. As expected, the measured PL intensity increased with increasing dopant molar percent concentrations, i.e. from 0.05 to 0.2 mol%, with 0.2 mol % evincing the highest PL red emission intensity observed. It is noteworthy that when the concentration was further increased to ~0.5 mol %, the PL signal apparently decreased, possibly due to a concentration quenching effect, wherein the Pr³⁺ acted as a trapping center and consequently, the excess energy dissipated non-radiatively.^{26, 51} As a result, in order to maximize signal-to-noise ratios and

therefore to acquire quantitative insights into as-obtained data, the acceptably performing 0.2 mol % Pr doped CaTiO_3 was used as the model system with which to subsequently attach MPA-capped CdSe QDs in order to observe potential charge and/or energy transfer behavior.

The steady state PL of MPA-capped CdSe QDs and of the complementary MPA-capped CdSe QD-porous CaTiO_3 : Pr heterostructures were collected upon excitation at 460 nm, shown in Figure 11A, a wavelength chosen in order to induce QD emission. This specific wavelength was primarily used to obtain the emission profile of only CdSe QDs themselves. At this wavelength, the absorption of CaTiO_3 is negligible, because the excitation energy at 460 nm is significantly lower than that needed to properly excite CaTiO_3 : Pr itself (i.e. 325 nm). According to Figure 11A, within experimental error, the PL intensity and position of the MPA-capped CdSe- CaTiO_3 : Pr heterostructure are similar to that of the MPA-capped CdSe QDs alone. Analogous optical behavior has been observed with our prior work on comparable MPA-capped CdSe- CaWO_4 heterostructures.³³

Upon excitation at 325 nm (Figure 11B), the as-obtained PL spectrum of the composite heterostructure exhibits a pair of emission peaks localized at 553 nm and 611 nm that can be ascribed to contributions from CdSe QDs and CaTiO_3 : Pr. It is evident that the PL spectrum of the composite heterostructure incorporates a convolution of signals derived from both constituent components. Moreover, when compared with the PL emission profile of each individual component subunit, namely CdSe and CaTiO_3 themselves, it is apparent that the PL intensities of all of the observed peaks within the heterostructure have been quenched to some extent. Comparable behavior has been previously observed with our analogous QD- CePO_4 : Tb systems in which we attributed the ‘quenching’ effect to charge transfer between CdSe and CePO_4 : Tb. By analogy, under 325 nm irradiation, it is plausible to postulate that the excited electrons within

the CB of CaTiO₃: Pr are transferred and favorably donated to the corresponding CB of CdSe QDs, thereby resulting in a reduction in the CaTiO₃: Pr³⁺ emission intensity within the resulting heterostructures themselves, since the CB of CaTiO₃ is higher in energy than the analogous CB of CdSe, as shown in Figure 16A.

Nonetheless, by contrast with the case of CePO₄ attached to QDs, the possibility of hole transfer from CdSe QDs to CaTiO₃: Pr in our current system herein is rather low, because the VB of our QDs is higher than that of the corresponding VB of CaTiO₃: Pr. Therefore, any observed quenching phenomena associated with our CdSe QDs upon 325 nm excitation would likely arise from either (i) an electron transfer (as opposed to a hole transfer) process emanating from CdSe to CaTiO₃: Pr or (ii) the possibility of a higher fraction of increased non-radiative decay processes. As highlighted in Figure 16A, the photo-generated electrons within CdSe QDs most likely possess a higher intrinsic energy as compared with the conduction band of CaTiO₃, a scenario which should give rise to plausible electron transfer.

It is worth mentioning that we have ruled out large and significant contributions from any possible energy transfer between CdSe and CaTiO₃. Indeed, as evinced by previous report⁵², in heterostructures incorporating either luminescent organic dyes or a bound system of inorganic materials and quantum dots, CdSe QDs nominally act as the energy transfer donors, if such a process is favored to occur at all. However, in our specific case, the spectral overlap between the emission spectra of CdSe QDs ($\lambda_{em} = 553$ nm) and the corresponding absorption spectra of CaTiO₃: Pr ($\lambda_{abs} \sim 325$ nm) is in fact rather minimal, and in effect, there is little if any overlap. Therefore, the energy transfer process in and of itself is unlikely to be a major contributor to the PL quenching within these heterostructures.

The excitation spectra of all of the individual components of these heterostructures have now been included in the Supplemental Information section, in order to better support our assertion that only charge transfer occurs within our composite system. As we have observed in Figures S7 and S8, the CdSe quantum dots do not appear to give rise to absorption at either 611 nm or 613 nm, namely the specific emission peak positions of Pr-CaTiO₃ and Eu-CaTiO₃, respectively. Similarly, neither Pr-CaTiO₃ nor Eu-CaTiO₃ can be excited by the absorption of light centered at 553 nm, which denotes the emission peak position of MPA-capped CdSe quantum dots. Because these 2 materials are excited at essentially very different wavelengths, it is likely that there is a lack of a spectral overlap (and hence, substantive interaction) between the underlying CaTiO₃ host and the immobilized CdSe QDs, thereby essentially ruling out the likelihood of energy transfer. We believe this assertion corroborates our overall narrative, and highlights the relatively greater role and importance of charge transfer herein.

3.3. Optical data collected on Eu-doped CaTiO₃ and Corresponding Heterostructures

PL emission spectra were collected on a complementary set of heterostructures, created from various molar percent concentrations (i.e. 'x' = 0, 2, 4, and 6) of a different dopant, i.e. Eu³⁺, within CaTiO₃, using an excitation wavelength of 397 nm, as shown in Figure 12. The characteristic Eu³⁺ emission bands located at 547, 590, 623, 650, and 692 nm can be assigned to a number of *f-f* transitions of the RE³⁺ ion, specifically the ⁵D₁-⁷F₁, ⁵D₀-⁷F₁, ⁵D₀-⁷F₂, ⁵D₀-⁷F₃, and ⁵D₀-⁷F₄ transitions, respectively, of Eu³⁺. By analogy, the PL intensity increased with increasing molar percent concentrations with a maximum observed with a 6 mol % material, i.e. yielding the highest PL red emission intensity observed. As a result, using this quantity as an 'optimal' composition, 6 mol % of Eu-doped CaTiO₃ was subsequently attached onto MPA-capped CdSe QDs in order to observe subsequent charge and energy transfer behavior.

Furthermore, this ‘optimal’ 6% Eu composition was taken as a ‘standard’ with which to draw comparisons with the optical properties of other perovskites including SrTiO₃, BaTiO₃, and CaTiO₃. For the PL spectra, the expected Eu³⁺ emission bands, corresponding to the *f-f* transitions, were observed for all of the perovskite titanate structures probed. However, from the collected PL spectra (Figure 13) of all of the various metal titanates analyzed, the Eu-doped CaTiO₃ evinced the highest measured PL red emission intensity.

From theoretical calculations, it has been postulated that this mid-sized rare earth metal undergoes an energetically favorable substitution with Ca, via a Ca oxygen vacancy within the CaTiO₃ host, whereas with BaTiO₃ and SrTiO₃, Eu can substitute at either the A or B sites.²⁰ Moreover, BaTiO₃ and SrTiO₃ appear to evince increasing binding energies for rare earth ion dopant cations of decreasing size.²⁰ Since Eu³⁺ is a medium-sized ion (~109 pm), it is plausible that the binding energy for Eu³⁺ is reduced within both Ba (~149 pm) and Sr (~118 pm) titanates with respect to CaTiO₃ (Ca²⁺ = ~132 pm and Ti⁴⁺ = 74.5 pm), and that therefore, the potential for Eu dopant incorporation is more favorable within the CaTiO₃ lattice. Hence, this phenomenon of an increased stabilization for Eu with the surrounding CaTiO₃ may possibly be due to not only the increased Coulombic attraction but also the higher charge density associated with the Ca vacancy for Eu³⁺.²⁰

In terms of the corresponding MPA-capped CdSe QD-CaTiO₃: Eu heterostructures (red curve), as indicated in Figures 14 and 16B, using an excitation wavelength of 399 nm, we noticed that the PL quenching of the CaTiO₃: Eu component is more significant and apparent, denoting behavior indicative of either (i) electron transfer occurring from CaTiO₃: Eu to the CdSe QDs or (ii) a larger proportion of competing non-radiative decay processes. By contrast, the quenching of the CdSe QDs themselves is almost negligible, especially by comparison with

the corresponding behavior of MPA-capped CdSe QD - CaTiO₃: Pr heterostructures. Indeed, due to the higher redox potential of MPA as compared with CdSe QDs and therefore unfavorable band alignment present, it is reasonable to assert that both the photoinduced holes trapped within MPA and the holes and electrons confined in QDs are not likely to migrate into CaTiO₃: Eu, thereby explaining the minimal reduction of the PL output associated with the CdSe QDs incorporated within these heterostructures.

4. Conclusions

Our work has elements of novelty in both synthesis and photophysics in an effort to predictively control optical behavior in nanoscale systems. Specifically, for the first time, a family of novel porous, crystalline, chemically pure, and micron-scale spherical motifs of CaTiO₃: Re (Pr and Eu), measuring ~200 to 350 nm in overall diameter and composed of individual constituent nanoparticles with diameters of ~30 to 40 nm, has been reliably prepared using both the molten salt as well as the hydrothermal methods. Based upon PL observations, our molten salt-derived samples evinced an increased red emission intensity possibly due to several factors, such as their slightly larger crystallite size, higher reaction temperature of formation, as well as greater surface area. Consequently, molten salt prepared samples CaTiO₃: were utilized with varying RE molar percentages in order to achieve the most 'optimized' photoluminescent material. Moreover, the optical behavior of Eu doped CaTiO₃ was compared with that of their related perovskites, i.e. BaTiO₃ and SrTiO₃, in order to observe the efficiency of each perovskite as a host material for the dopant substituent Eu³⁺ ion.

Based upon PL measurements, amongst the samples tested, it was observed that CaTiO₃ served as the most appropriate host for Eu, due to an increased Coulombic attraction and a higher

charge density for the dopant ion. As a result, ‘optimized’ concentrations of 0.2 and 6 mol % of Pr and Eu-doped CaTiO_3 structures, respectively, were decorated with CdSe QDs in order to observe and account for novel energy and charge transfer behaviors. In terms of the optical properties of the as-prepared heterostructures, enhancements of PL intensities were noted upon excitation under UV-visible light (i.e. 460 nm), owing to the surface passivation effect.

Nevertheless, the predominant storyline within the heterostructures themselves was the observation of effective charge transfer and/or non-radiative decay processes from CdSe to CaTiO_3 and vice versa, as verified by quenching effects of the PL profiles associated with the individual constituent components. In addition, due to the distinctive alignment of energy levels associated with the two discrete dopants, we found that the CaTiO_3 : Pr and CaTiO_3 : Eu yielded dissimilar but nevertheless fundamentally predictable quenching behaviors. In effect, the optical behavior of the heterostructures was effectively controlled by the luminescence properties of the activators, the host lattice, and the QDs as well as by their relative energy band level alignment.

5. Acknowledgements:

Research for all authors was supported by the U.S. Department of Energy, Basic Energy Sciences, Materials Sciences and Engineering Division. Experiments for this manuscript were performed in part at the Center for Functional Nanomaterials located at Brookhaven National Laboratory, which is supported by the U.S. Department of Energy under Contract No. DE-AC02-98CH10886 and DE-SC-00112704.

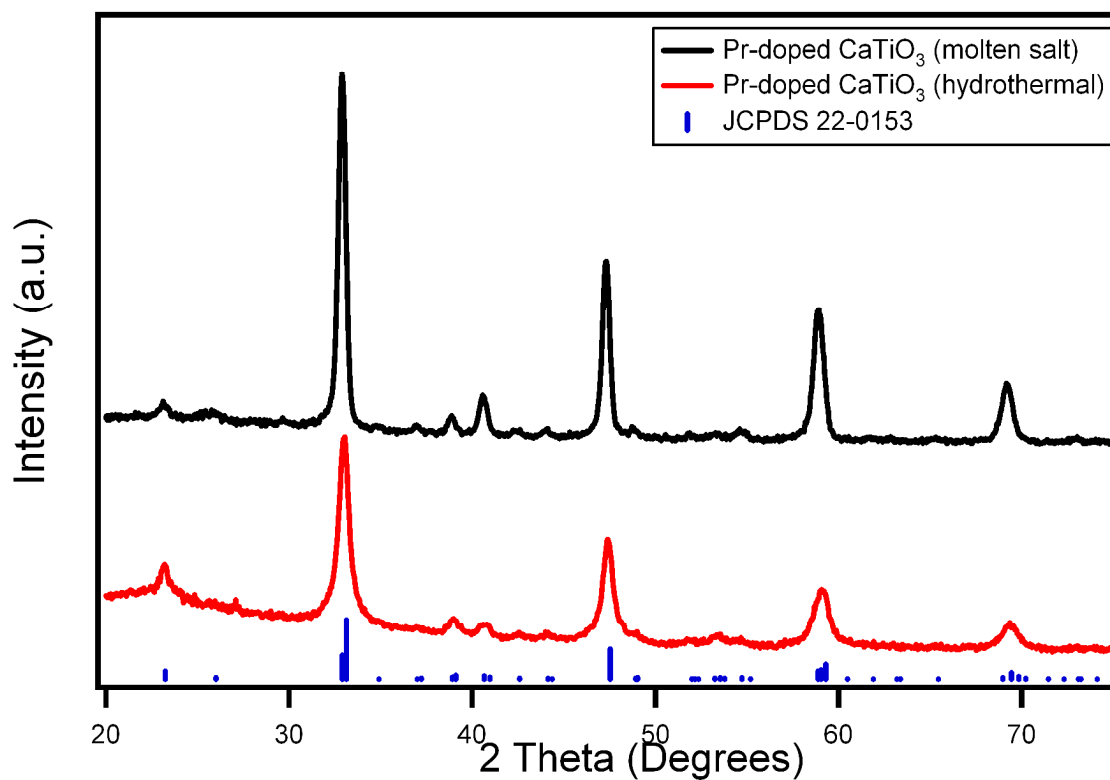


Figure 1. XRD patterns of as-prepared, luminescently desirable 0.2 molar percent Pr-doped CaTiO₃ microspheres, generated via molten salt (top, black) and hydrothermal (middle, red) methodologies. The JCPDS no. 22-0153 database standard is shown for the bulk orthorhombic perovskite, CaTiO₃ (bottom, blue).

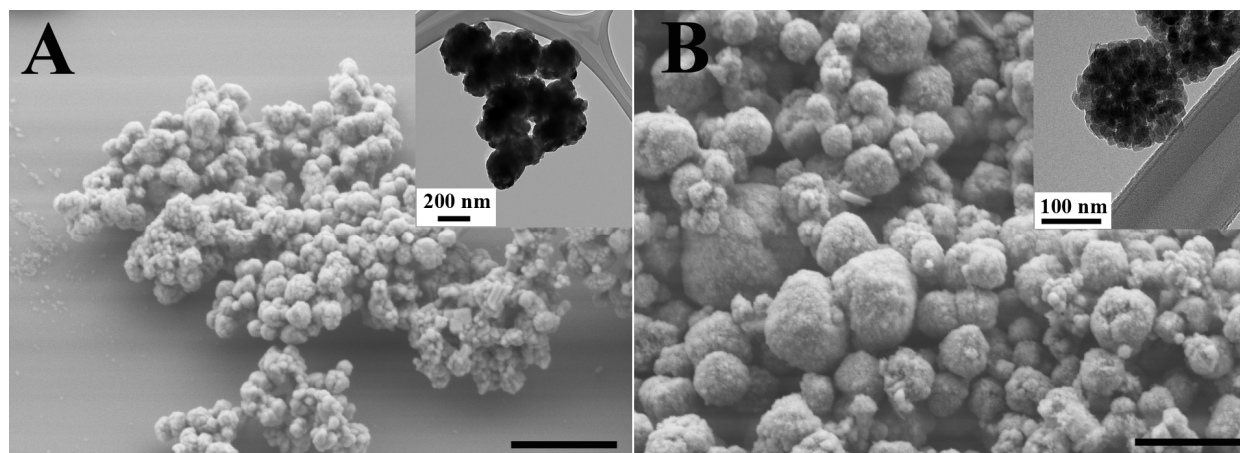


Figure 2. Representative SEM images of (A) molten salt-derived Pr-CaTiO₃ and (B) hydrothermally-treated Pr-CaTiO₃ with the corresponding TEM images highlighted in the insets to (A) and (B). Scale bar is 1 μm for each SEM image shown.

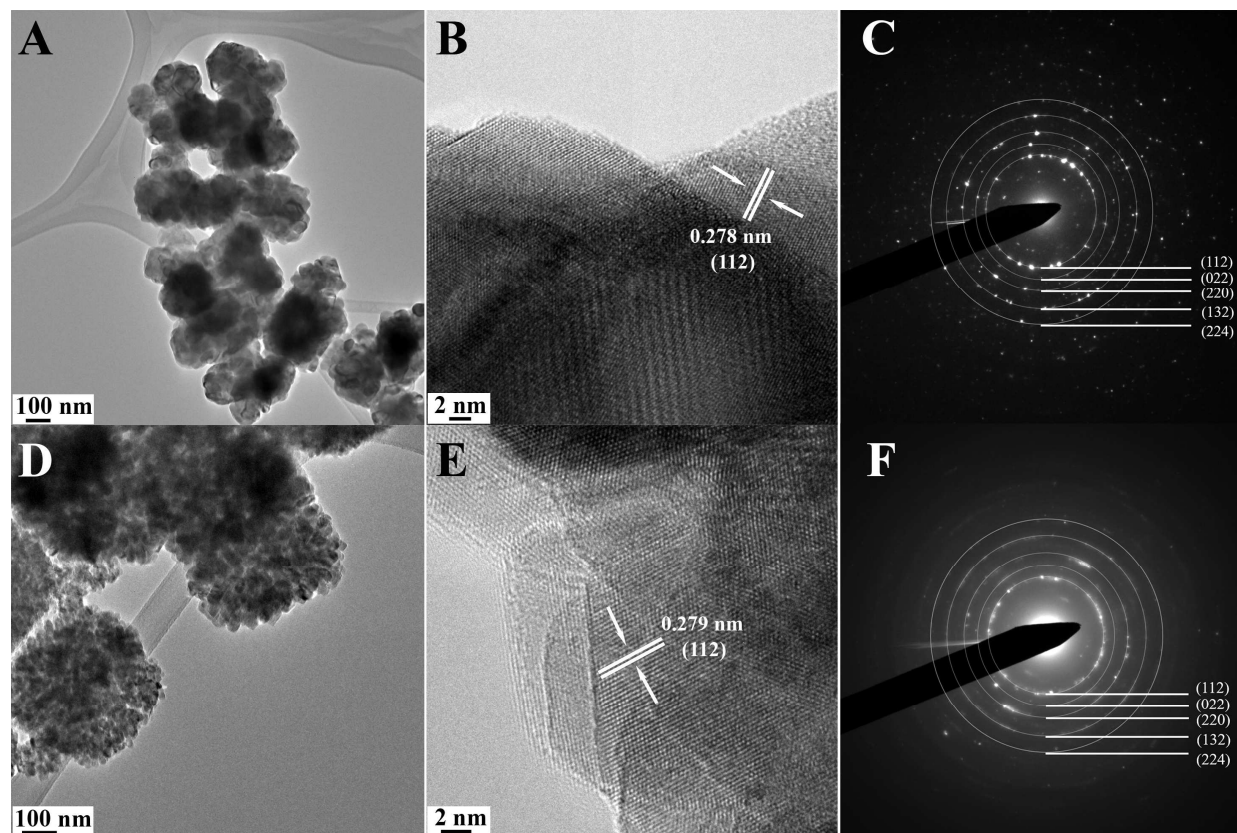


Figure 3. Representative (A and D) TEM and (B and E) HR-TEM images, as well as the corresponding SAED (C and F) patterns, associated with bare Pr-CaTiO₃ prepared using both molten salt and hydrothermal methods, respectively.

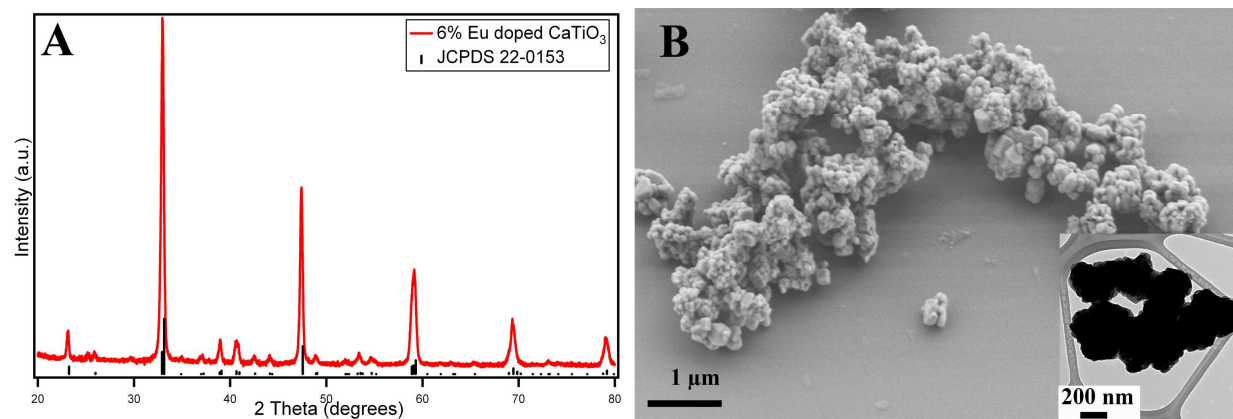


Figure 4. Representative (A) XRD pattern, as well as (B) SEM and (inset of B) TEM images of Eu-doped CaTiO₃, prepared using the molten salt technique.

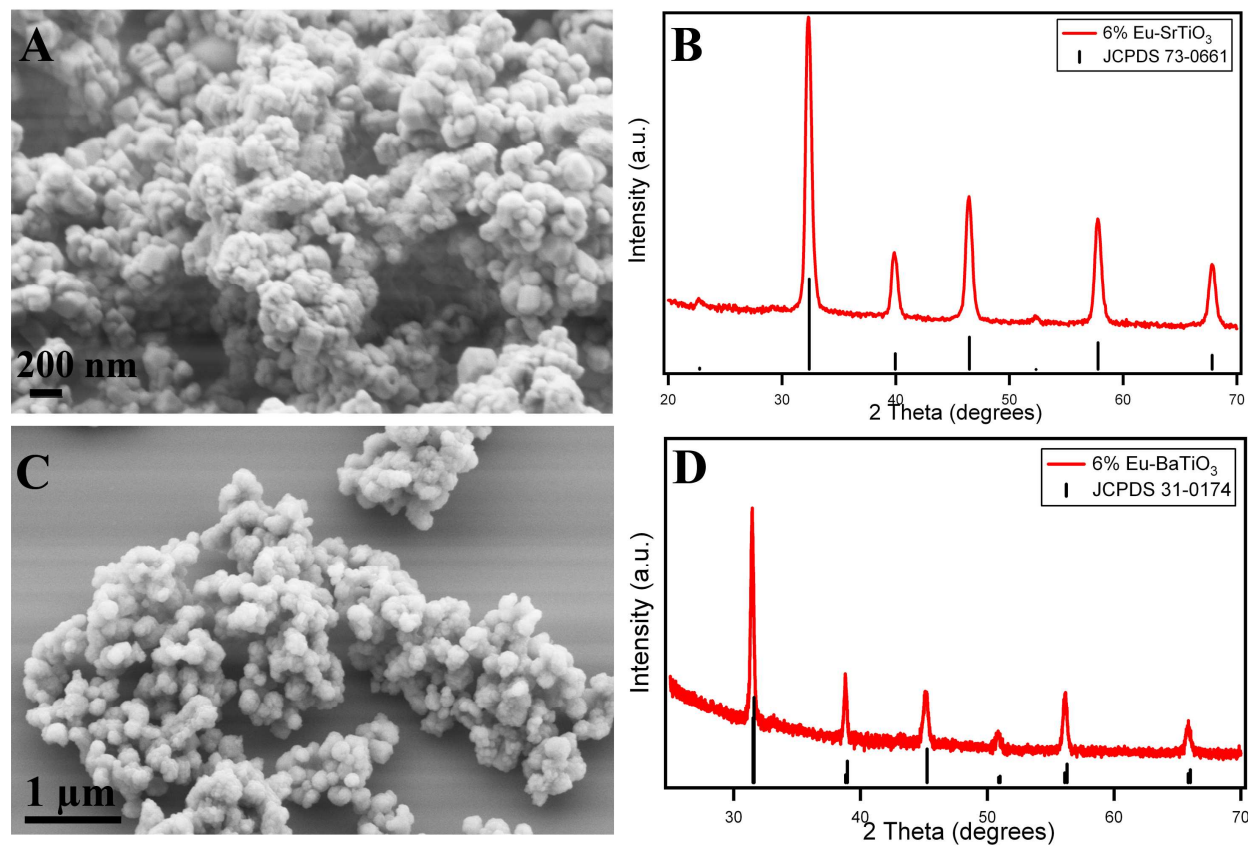


Figure 5. Representative SEM (A and C) and XRD patterns (B and D) of Eu-doped SrTiO₃ and BaTiO₃, respectively, using the molten salt synthesis technique.

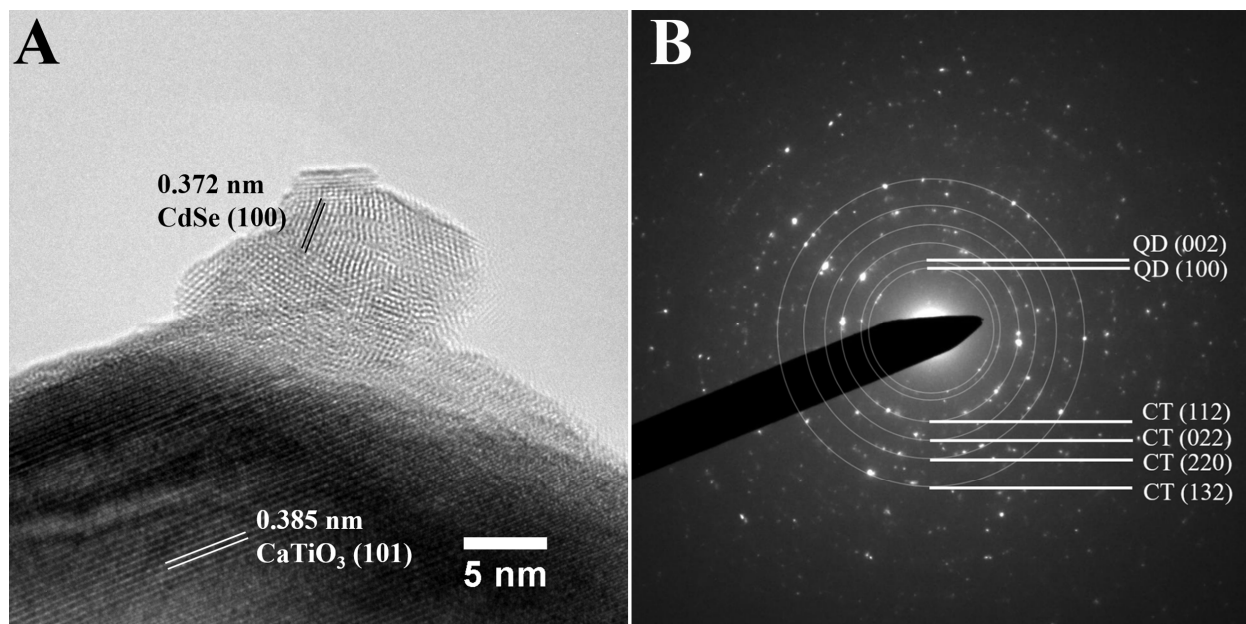


Figure 6. Representative (A) HR-TEM image as well as the corresponding SAED (B) pattern, associated with heterostructures composed of CdSe QD attached onto Pr-doped CaTiO₃ porous spherical motifs.

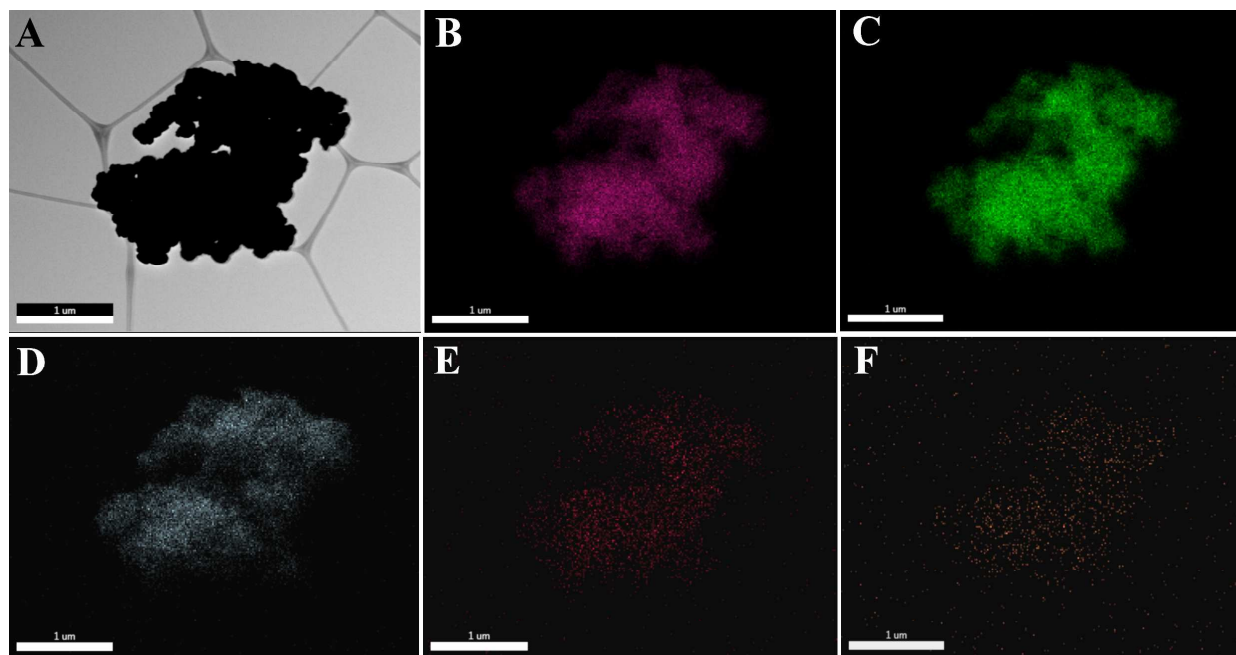


Figure 7. (A) Dark-field STEM image of CdSe QDs anchored onto CaTiO₃: Pr heterostructures. Elemental mapping of the same region as measured by energy dispersive X-ray spectroscopy, highlighting the spatial elemental distribution of (B) Ca, (C) Ti, (D) O, (E) Cd, and (F) Se, respectively. Scale bar is 1 μm for each image.

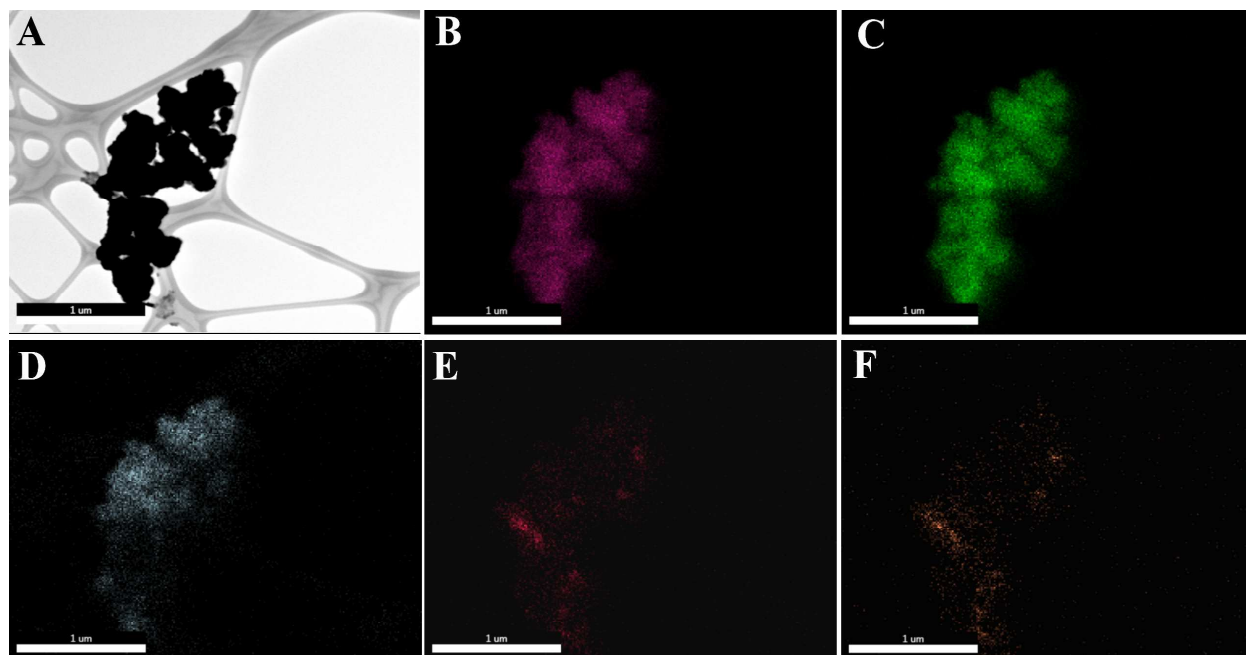


Figure 8. (A) Dark-field STEM image of CdSe QDs anchored onto CaTiO₃: Eu heterostructures. Elemental mapping of the same region as measured by energy dispersive X-ray spectroscopy, highlighting the spatial elemental distribution of (B) Ca, (C) Ti, (D) O, (E) Cd, and (F) Se, respectively. Scale bar is 1 μm for each image.

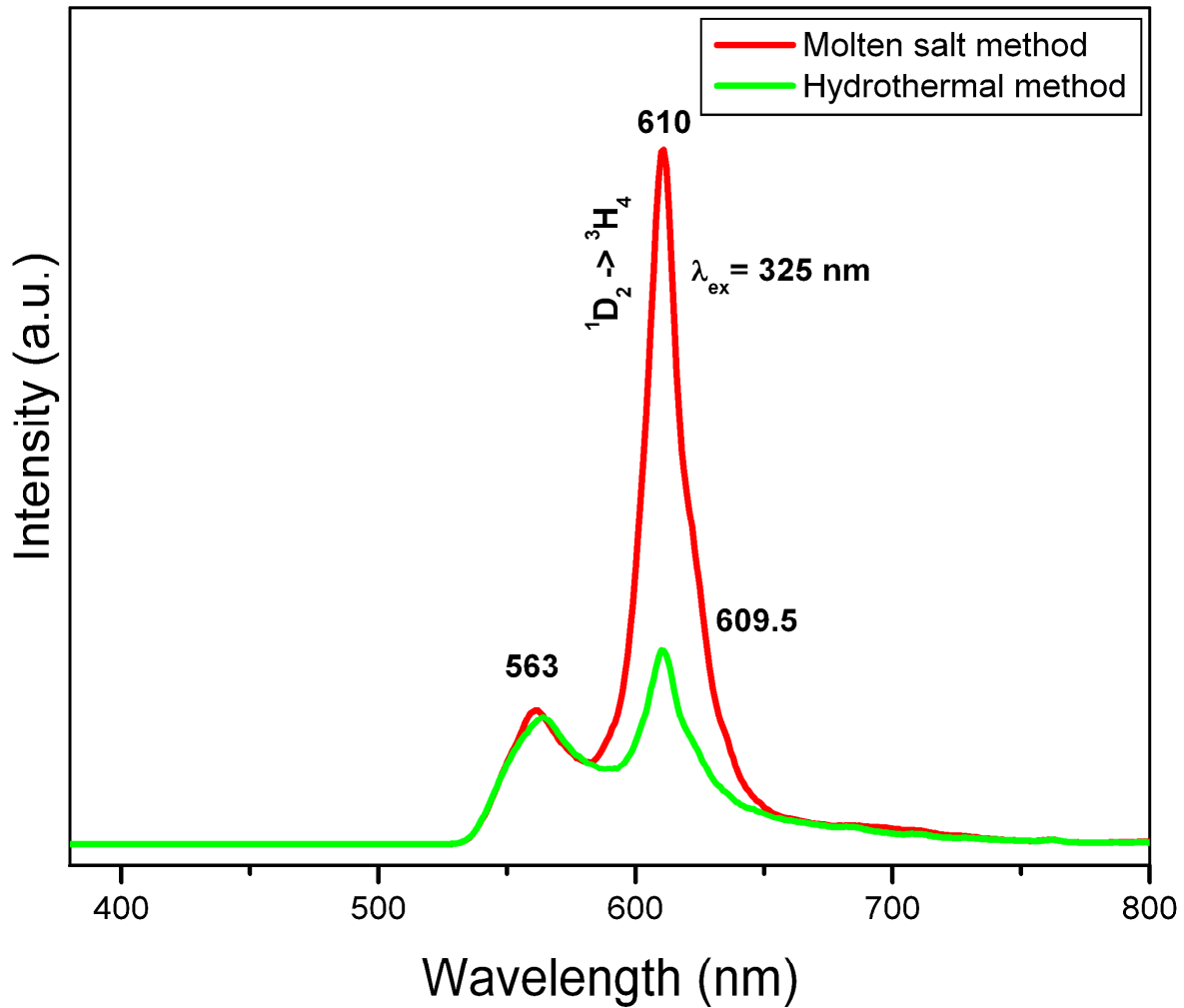


Figure 9. Photoluminescence emission of 0.2 mol % Pr³⁺-doped-CaTiO₃ prepared by molten salt and hydrothermal methods, respectively, and collected at an excitation wavelength of 325 nm.

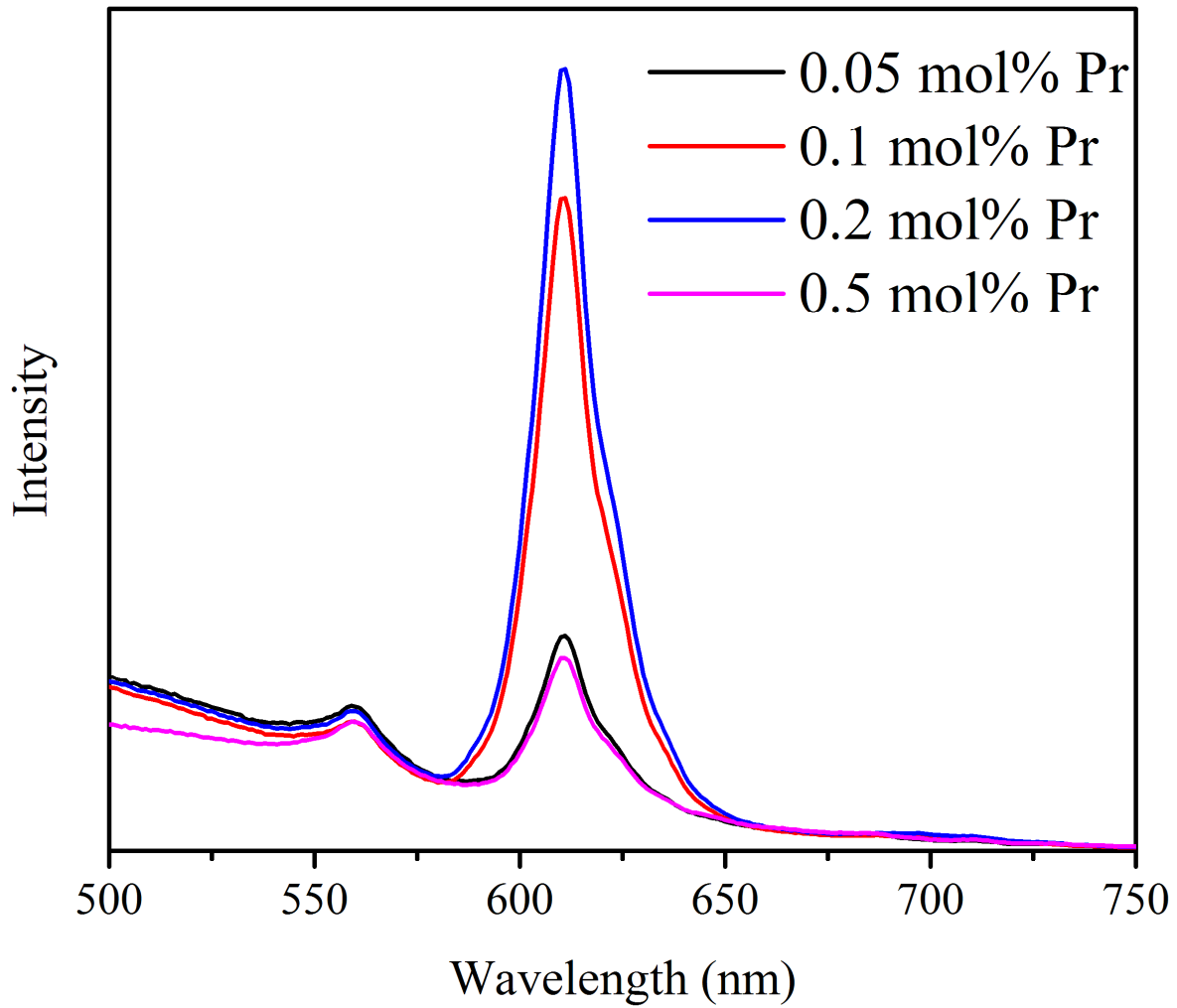


Figure 10. Photoluminescence emission data collected with various concentrations of Pr^{3+} -doped CaTiO_3 prepared using the molten salt reaction protocol and acquired at an excitation wavelength of 325 nm.

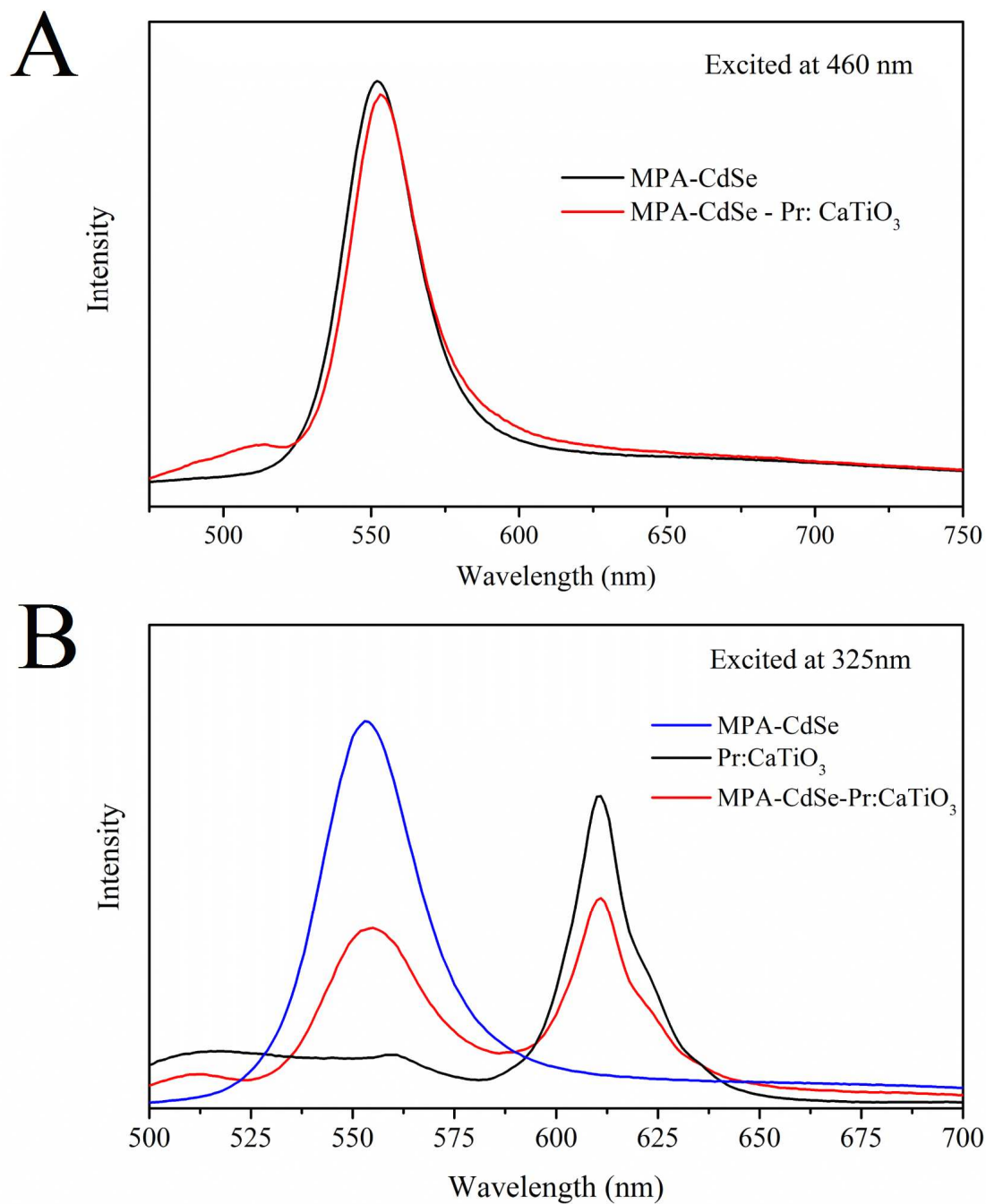


Figure 11. PL emission spectra of MPA-capped CdSe QDs, CaTiO₃: Pr, as well as MPA-capped CdSe QD -CaTiO₃: Pr heterostructures under (A) 460 and (B) 325 nm excitation, respectively.

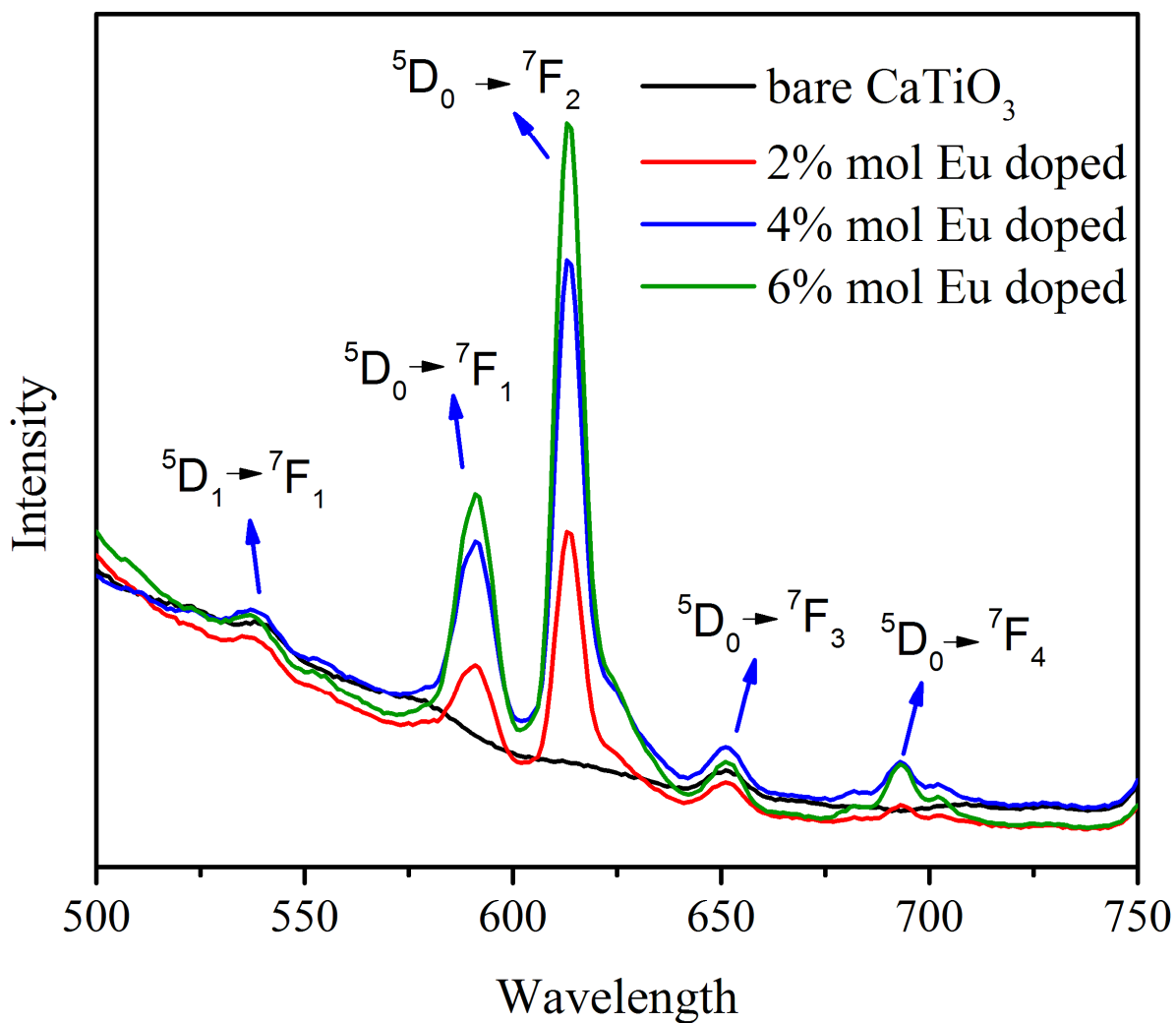


Figure 12. PL emission spectra of various molar % concentrations (i.e. 0, 2, 4, and 6%) of Eu-doped CaTiO₃, prepared using the molten salt method. Data were collected at an excitation wavelength of 399 nm.

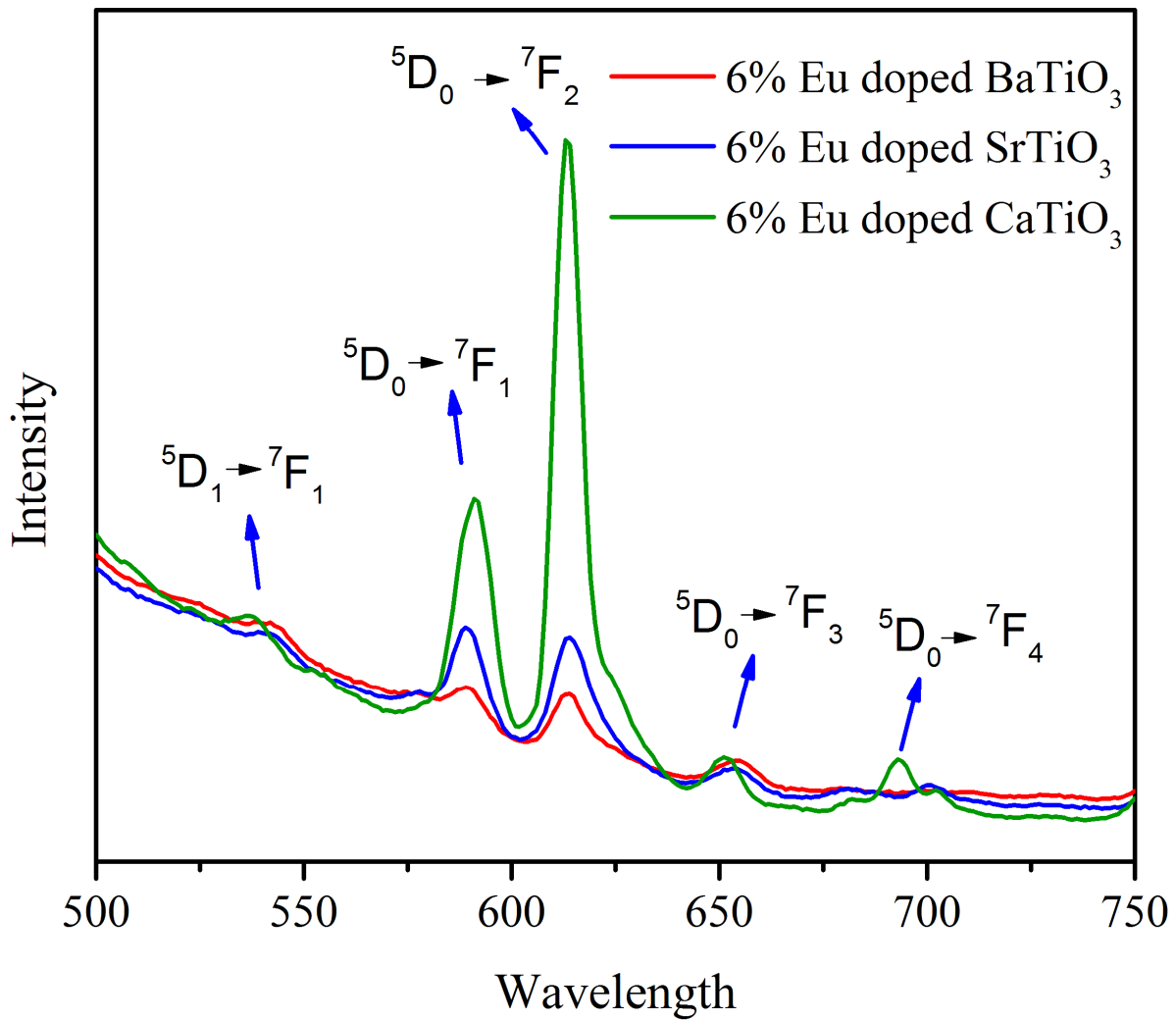


Figure 13. PL emission spectra obtained at 6 mol % concentrations of Eu-doped CaTiO₃, BaTiO₃, and SrTiO₃, prepared using the molten salt method. Data were collected at an excitation wavelength of 399 nm.

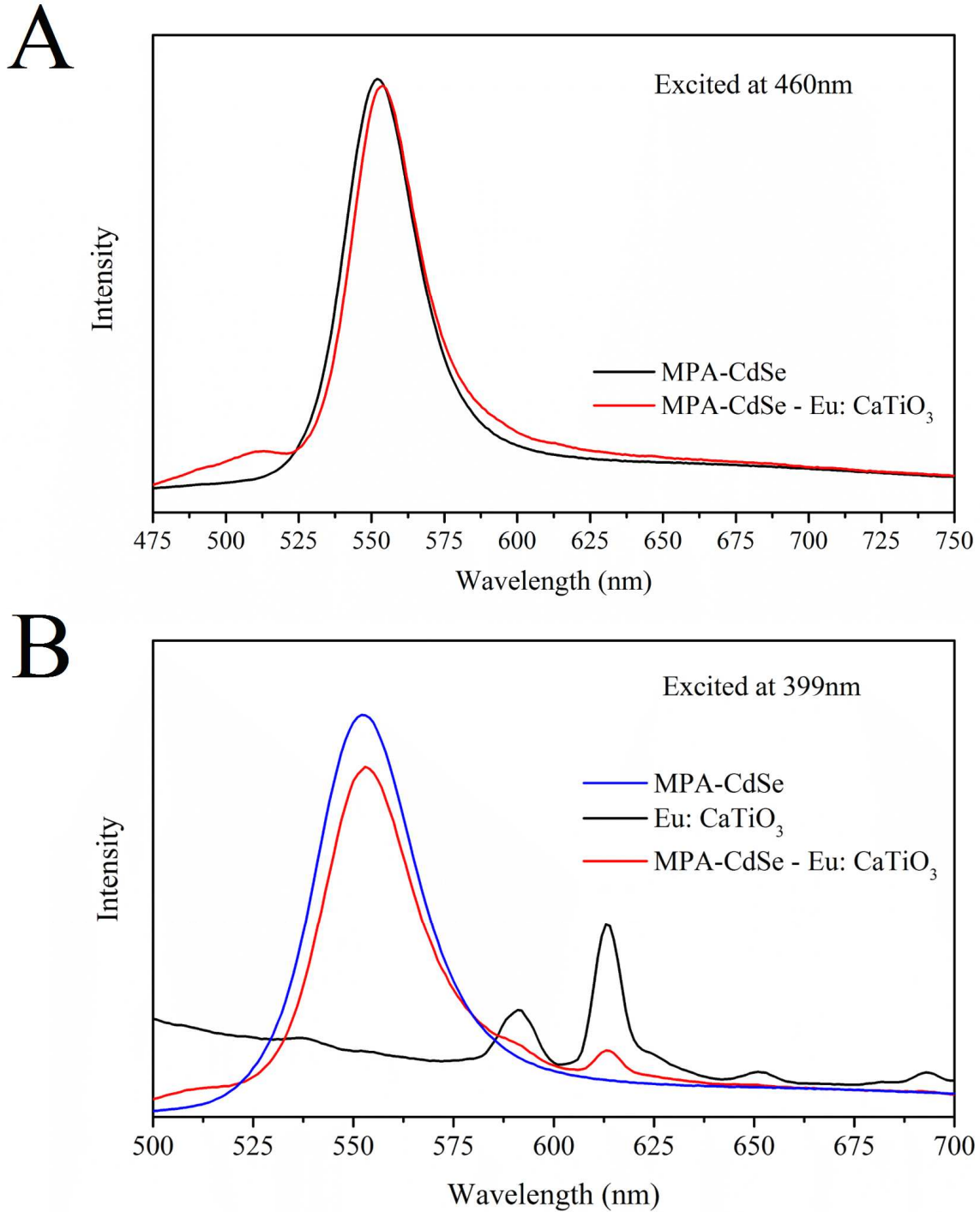


Figure 14. PL emission spectra of MPA-capped CdSe QDs, CaTiO₃: Eu, as well as MPA-capped CdSe-CaTiO₃: Eu heterostructures under (A) 460 and (B) 399 nm excitation, respectively.

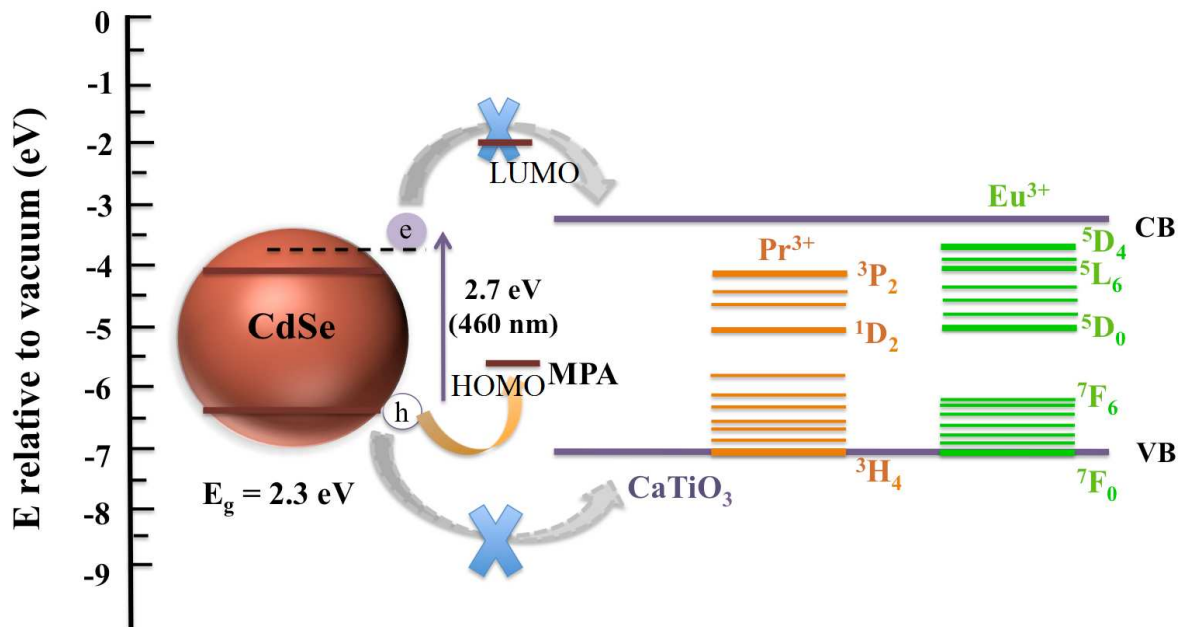


Figure 15. Potential electronic energy diagram, illustrating the energy band alignments associated with CdSe QDs anchored onto CaTiO₃ doped with Pr and with Eu, under an excitation of 460 nm incident light. CB = conduction band; VB = valence band; LUMO = lowest unoccupied molecular orbitals; and HOMO = highest occupied molecular orbitals.

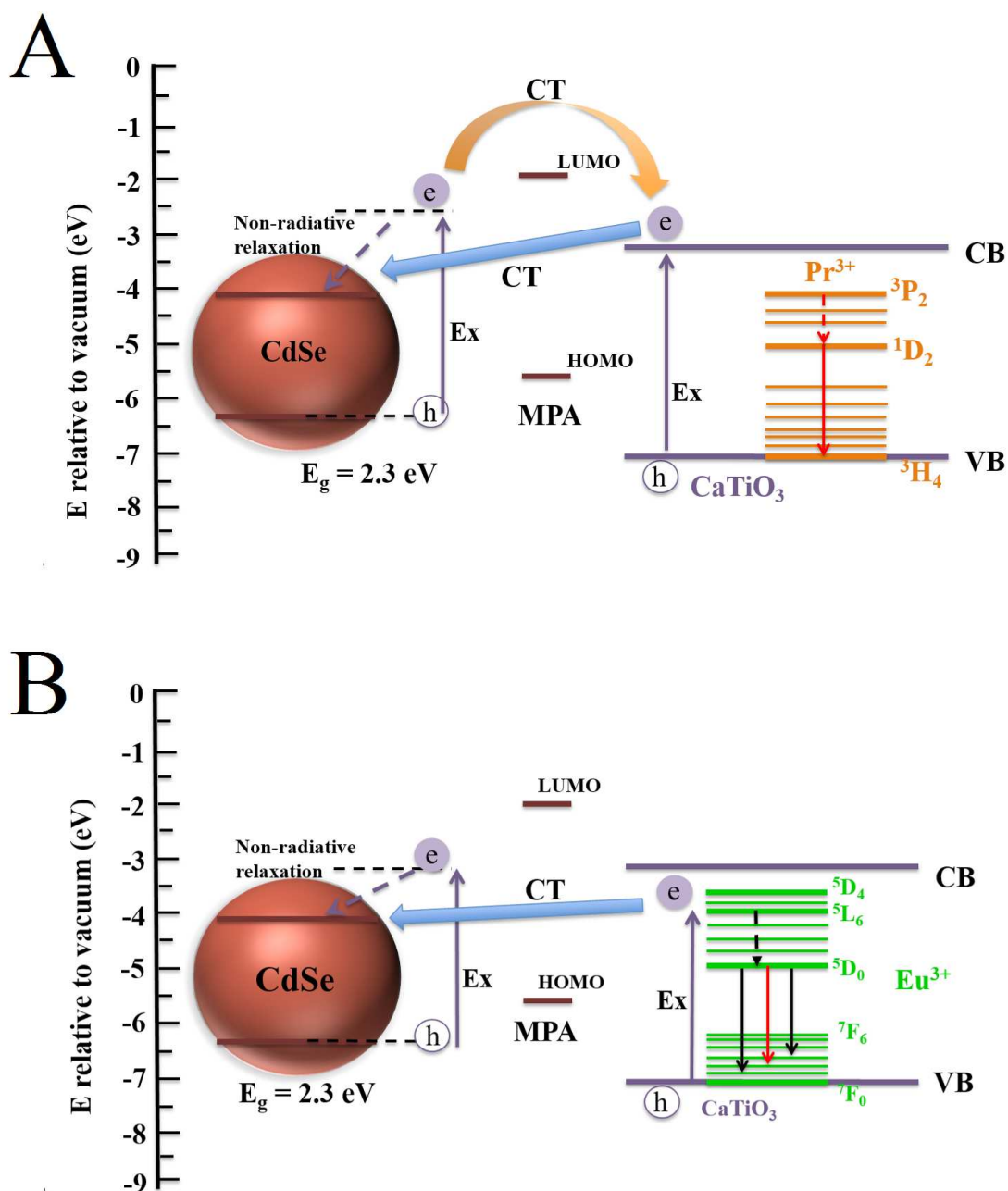
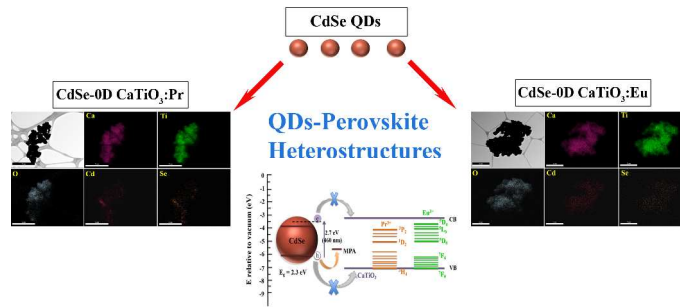


Figure 16. Potential electronic energy diagram, illustrating the energy band alignments associated with CdSe QDs anchored onto CaTiO₃ doped with Pr and with Eu, as well as the potential for corresponding charge transfer (CT), taking place within the heterostructure, under the excitation of 325 nm (panel A) and 399 nm (panel B), respectively. CB = conduction band; VB = valence band; LUMO = lowest unoccupied molecular orbitals; and HOMO = highest occupied molecular orbitals.



TOC Figure. RE (RE = Eu and Pr) doped CaTiO₃ were synthesized using facile molten salt and hydrothermal methodologies. These perovskites were subsequently immobilized with CdSe QDs and the heterostructures evinced charge transfer between the host material (CaTiO₃) and the attached QDs.

References

1. Y. Mao, S. Banerjee and S. S. Wong, *Journal of the American Chemical Society*, 2003, **125**, 15718-15719.
2. J. Shi and L. Guo, *Progress in Natural Science: Materials International*, 2012, **22**, 592-615.
3. S. Stolen, E. Bakken and C. E. Mohn, *Physical Chemistry Chemical Physics*, 2006, **8**, 429-447.
4. F. A. Rabuffetti and R. L. Brutchey, *Dalton Transactions*, 2014, **43**, 14499-14513.
5. J. Zhu, H. Li, L. Zhong, P. Xiao, X. Xu, X. Yang, Z. Zhao and J. Li, *ACS Catalysis*, 2014, **4**, 2917-2940.
6. J. Kaur, V. Dubey, Y. Parganiha, D. Singh and N. S. Suryanarayana, *Research on Chemical Intermediates*, 2015, **41**, 3597-3621.
7. X. Zhang, J. Zhang, Y. Jin, H. Zhao and X.-j. Wang, *Crystal Growth & Design*, 2008, **8**, 779-781.
8. C. N. George, J. K. Thomas, R. Jose, H. P. Kumar, M. K. Suresh, V. R. Kumar, P. R. S. Wariar and J. Koshy, *Journal of Alloys and Compounds*, 2009, **486**, 711-715.
9. D. Wang, Y. Liu, H. Hu, Z. Zeng, F. Zhou and W. Liu, *The Journal Of Physical Chemistry C*, 2008, **112**, 16123-16129.
10. A. L. Tiano, A. C. Santulli, C. Koenigsmann, M. Feygenon, M. C. Aronson, R. Harrington, J. B. Parise and S. S. Wong, *Chemistry of Materials*, 2011, **23**, 3277-3288.
11. A. C. Santulli, H. Zhou, S. Berweger, M. B. Raschke, E. Sutter and S. S. Wong, *Crystal Engineering Communications*, 2010, **12**, 2675-2678.
12. T.-J. Park, Y. Mao and S. S. Wong, *Chemical Communications*, 2004, **23**, 2708-2709.
13. S. B. Yuanbing Mao, and Stanislaus S. Wong, *Journal of the American Chemical Society*, 2003, **125**, 15718-15719.
14. Y. Mao, S. Banerjee and S. S. Wong, *Chemical Communications*, 2003, **3**, 408-409.
15. K. Asami, K. Saito, N. Ohtsu, S. Nagata and T. Hanawa, *Surface and Interface Analysis*, 2003, **35**, 483-488.
16. K. Asami, N. Ohtsu, K. Saito and T. Hanawa, *Surface and Coatings Technology*, 2005, **200**, 1005-1008.
17. S. Som, A. K. Kunti, V. Kumar, V. Kumar, S. Dutta, M. Chowdhury, S. K. Sharma, J. J. Terblans and H. C. Swart, *Journal of Applied Physics*, 2014, **115**, 193101/193101-193101/193114.
18. H. Takashima, K. Ueda and M. Itoh, *Applied Physics Letters*, 2006, **89**, 261915/261911-261915/261913.
19. L. S. Cavalcantea, V. S. Marquesb, J. C. Sczancoskia, M. T. Escotec, M. R. Joyaa, J. A. Varelada, M. R. M. C. Santosb, P. S. Pizania and E. Longod, *Chemical Engineering Journal*, 2008, **143**, 299-307.
20. J. A. Dawson, X. Li, C. L. Freeman, J. H. Harding and D. C. Sinclair, *Journal of Materials Chemistry C*, 2013, **1**, 1574-1582.
21. V. V. Lemanov, A. V. Sotnikov, E. P. Smirnova and M. Weihnacht, *Applied Physics Letters*, 2002, **81**, 886-888.
22. E. Korkmaz and N. O. Kalaycioglu, *Journal of the Chinese Chemical Society*, 2012, **59**, 1390-1393.

23. K. Goto, Y. Nakachi and K. Ueda, *Thin Solid Films*, 2008, **516**, 5885-5889.
24. M. Upadhyay Kahaly and U. Schwingenschlogl, *Journal of Materials Chemistry A: Materials for Energy and Sustainability*, 2014, **2**, 10379-11383.
25. A. K. Levine and F. C. Palilla, *Applied Physics Letters*, 1964, **5**, 118.
26. C. Peng, Z. Hou, C. Zhang, G. Li, H. Lian, Z. Cheng and J. Lin, *Optics Express*, 2010, **18**, 7543-7551.
27. K. Minami, Y. Hakuta, M. Ohara, M. Aoki, K. Sue and H. Takashima, *ECS Transactions*, 2013, **50**, 19-24.
28. A. Isobe, S. Takeshita and T. Isobe, *Langmuir*, 2015, **31**, 1811-1819.
29. X. Peng, M. Y. Sfeir, F. Zhang, J. A. Misewich and S. S. Wong, *Journal of Physical Chemistry C*, 2010, **114**, 8766-8773.
30. X. Peng, J. A. Misewich, S. S. Wong and M. Y. Sfeir, *Nano Letters*, 2011, **11**, 4562-4568.
31. J. Han, L. Wang and S. S. Wong, *RSC Advances*, 2014, **4**, 34963-34980.
32. J. Han, L. Wang and S. S. Wong, *The Journal Of Physical Chemistry C*, 2014, **118**, 5671-5682.
33. J. Han, C. McBean, L. Wang, J. Hoy, C. Jaye, H. Liu, Z.-Q. Li, M. Y. Sfeir, D. A. Fischer, G. T. Taylor, J. A. Misewich and S. S. Wong, *Chemistry of Materials*, 2015, **27**, 778-792.
34. J. Han, C. McBean, L. Wang, C. Jaye, H. Liu, D. A. Fischer and S. S. Wong, *Journal of Physical Chemistry C*, 2015, **119**, 3826-3842.
35. Z. Zhang, X. Li, C. Gao, F. Teng, Y. Wang, L. Chen, W. Han, Z. Zhang and E. Xie, *Journal of Materials Chemistry A: Materials for Energy and Sustainability*, 2015, **3**, 12769-12776.
36. G. Sreedhar, A. Sivanantham, S. Venkateshwaran, S. K. Panda and M. Eashwar, *Journal of Materials Chemistry A: Materials for Energy and Sustainability*, 2015, **3**, 13476-13482.
37. T. S. Malyy, V. V. Vistovskyy, Z. A. Khapko, A. S. Pushak, N. E. Mitina, A. S. Zaichenko, A. V. Gektin and A. S. Voloshinovskii, *Journal of Applied Physics*, 2013, **113**, 224305/224301-224305/224307.
38. J. Zhang, N. Zhang, L. Zou and S. Gan, *RSC Advances*, 2014, **4**, 38455-38465.
39. L. Qu and X. Peng, *Journal of the American Chemical Society*, 2002, **124**, 2049-2055.
40. J. Fu, Q. Zhang, Y. Li and H. Wang, *Journal of Luminescence*, 2009, **130**, 231-235.
41. M. R. Mohammadi and D. J. Fray, *Journal of Sol-Gel Science and Technology*, 2013, **68**, 324-333.
42. S. Fuentes, N. Barraza, E. Veloso, R. Villarroel and J. Llanos, *Journal of Alloys and Compounds*, 2013, **569**, 52-57.
43. Z. Sun, G. Cao, Q. Zhang, Y. Li and H. Wang, *Materials Chemistry and Physics*, 2012, **132**, 215-221.
44. G. Huang, W. Dong, L. Fang, F. Zheng and M. Shen, *Journal of Advanced Dielectrics*, 2011, **1**, 215-221.
45. X. Zhang, J. Zhang, Y. Jin, H. Zhao and X.-j. Wang, *Crystal Growth & Design*, 2009, **8**, 779-781.
46. X. Zhang, J. Zhang, X. Zhang, M. Wang, H. Zhao, S. Lu and X.-j. Wang, *Journal of Physical Chemistry C*, 2007, **111**, 18044-18048.
47. A. Purwanto, D. Hidayat, Y. Terashi and K. Okuyama, *Chemistry of Materials*, 2008, **20**, 7440-7446.

48. C. M. Lau, X. Wu and K. W. Kwok, *Journal of Applied Physics*, 2015, **118**, 034107/034101-034107/034107.
49. M. L. Moreira, E. C. Paris, G. S. do Nascimento, V. M. Longo, J. R. Sambrano, V. R. Mastelaro, M. I. B. Bernardi, J. Andres, J. A. Varela and E. Longo, *Acta Materialia*, 2009, **57**, 5174-5185.
50. J. Li, Y. C. Zhang, T. X. Wang and M. Zhang, *Materials Letters*, 2011, **65**, 1556-1558.
51. B. Mari, K. C. Singh, P. Cembrero-Coca, I. Singh, D. Singh and S. Chand, *Displays*, 2013, **34**, 346-351.
52. R. C. Somers, M. G. Bawendi and D. G. Nocera, *Chem Soc Rev*, 2007, **36**, 579-591.